Journal of Colloid and Interface Science 537 (2019) 465–474

Contents lists available at ScienceDirect

Journal of Colloid and Interface Science

journal homepage: www.elsevier.com/locate/jcis

Preferential adsorption of selenium oxyanions onto {1 1 0} and {0 1 2} nano-hematite facets

Amanda W. Lounsbury [a,b,*], Ranran Wang [c], Desiree L. Plata [a], Nicholas Billmyer [a], Christopher Muhich [d,e], Kiyoshi Kanie [f], Tadao Sugimoto [f], Derek Peak [g], Julie B. Zimmerman [a,b,h]

[a] Yale University, Department of Chemical and Environmental Engineering, New Haven, CT 06511, United States
[b] Nanosystems Engineering Research Center for Nanotechnology-Enabled Water Treatment, Yale University, United States
[c] University of Twente, Faculty of Engineering Technology, Enschede, 7500 AE, Netherlands
[d] Arizona State University, School for the Engineering of Matter, Transport and Energy, Ira A Fulton Schools of Engineering, Tempe, AZ 85001, United States
[e] Nanosystems Engineering Research Center for Nanotechnology-Enabled Water Treatment, Arizona State University, United States
[f] Institute for Multidisciplinary Research and Advanced Materials Processing, Tohoku University, Sendai, Japan
[g] University of Saskatchewan, Dep. of Soil Science, Saskatoon, SK S7N 5A8, Canada
[h] Yale University School of Forestry and Environmental Studies, New Haven, CT 06511, United States

GRAPHICAL ABSTRACT

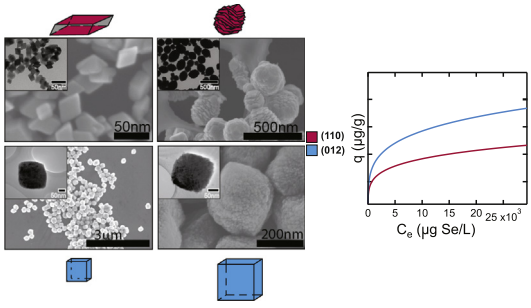

ARTICLE INFO

Article history:
Received 28 July 2018
Revised 2 November 2018
Accepted 7 November 2018
Available online 13 November 2018

Keywords:
Adsorption
Selenium (Se)
Hematite (α-Fe_2O_3)
Nanoparticle

ABSTRACT

As the commercial use of nano metal oxides, including iron oxides, becomes more prevalent, there is a need to understand functionality as it relates to the inherent properties of the nanomaterial. Many applications of nanomaterials rely on adsorption, ranging from catalysis to aqueous remediation. In this paper, adsorption of selenium (Se), an aqueous contaminant, is used as a model sorbate to elucidate the relationships of structure, property, and (adsorptive) function of nano-hematite (nα-Fe_2O_3). As such, six nα-Fe_2O_3 particles were synthesized controlling for size, shape and surface area without capping agents. Sorbent characteristics of the six particles were then assessed for their impact on selenite ($HSeO_3^-$) and selenate (SeO_4^{2-}) adsorption capacity and mechanism. Mechanism was assessed using *in-situ* attenuated total reflectance-Fourier transform infrared (ATR-FTIR) spectroscopy and extended X-ray absorption fine edge spectroscopy (EXAFS). Regression analyses were then performed to determine which characteristics best describe adsorption capacity and binding mechanisms of Se on nα-Fe_2O_3. The results demonstrate that crystal surface structure, specifically presence of the {0 1 2} facet promotes adsorption of Se and the presence of {0 1 2} facets promotes SeO_4^{2-} sorption to a greater extent than $HSeO_3^-$. The data further indicates that {1 1 0} facets bind $HSeO_3^-$ with binuclear complexes while {0 1 2} facets bind $HSeO_3^-$ via mononuclear inner-sphere complexes. Specific nα-Fe_2O_3 facets also likely direct the ratio of inner to outer-sphere complexes in SeO_4^{2-} adsorption.

* Corresponding author at: 17 Hillhouse Ave, 5th Floor, New Haven, CT 06510, United States.
E-mail address: amanda.lounsbury@yale.edu (A.W. Lounsbury).

https://doi.org/10.1016/j.jcis.2018.11.018
0021-9797/

1. Introduction

Nanomaterials in technological applications is an emerging global market, projected to reach $3 trillion by 2020 [1]. Like all technologies, to achieve greatest market value, nanotechnologies should be designed to maximally attain their defined functional role [2] and simultaneously minimize unintended hazards [3]. Currently, improving desired behavior for application and reducing undesirable behavior for implications remains an expensive and intensive empirical exercise [4–6]. The Structure-Property-Function and Structure-Property-Hazard framework (SPF-SPH) [3] allows for a fundamental understanding of the components that drive behavior such that nanotechnology can be efficaciously designed to optimize function and minimize hazard.

Adsorption is an essential function, necessary for applications in analytical chemistry [7], catalysis [8,9], gas-sensing [10,11], biomedical applications [12], and environmental remediation [13]. Capacity and mechanism comprise the what and how of adsorption behavior, and are each important for improved design under the SPF-SPH framework. Of the available adsorbent technologies, nano-adsorbents, and specifically nano-metal oxides (NMO), including iron oxides, present an opportunity for enhanced performance over their bulk counterparts due to the relative increase in surface area to mass ratio of the nanomaterials [14,15].

In the nano-regime, an increase in surface area (and thus smaller particle sizes) is also conventionally thought to enhance adsorption capacity [16], yet, evidence suggests, this is not necessarily the case [17–20]. Differences in adsorption of selenite between goethite particles of similar surface area have been reported [21,22]. Torrent et al. also found different phosphate adsorption capacities onto goethite crystals [17]. While, the former attributed the variation in adsorption to differences in point of zero charge (pzc) of the particles, Torrent et al. suggests crystal facet and defects formed by polydomaine surfaces are responsible. Similarly, Lounsbury et al. hypothesizes that surface functional groups are responsible for enhanced adsorption capacity of selenium oxyanions onto nano-hematite (nα-Fe_2O_3) rather than increased nα-Fe_2O_3 surface area [19]. Madden et al. attributes increased Cu^{2+} adsorption onto smaller (7 nm) nα-Fe_2O_3 than larger (25 nm and 80 nm) particles to the increased proportion of distorted binding sites on the smaller particles [23]. Recently, Huang et al. examined the adsorption capacity and mechanism of Cr(VI) onto two nα-Fe_2O_3 particles with two different frontier facets [24]. The authors report that Cr(VI) adsorption capacity is higher on {1 1 0} facets with bidentate binuclear complexes than on the {0 0 1} facet with monodentate mononuclear complexes [24]. This suggests that similarly to bulk adsorbents, both adsorption capacity and complexation mechanism are facet dependent for nano-adsorbents; however, size and surface area were not controlled or evaluated [24]. Therefore, towards development of an SPF relationship for adsorption, the specific nano-properties and characteristics responsible for adsorption capacity and mechanism are limited. The need for more information is exacerbated by nano-properties and characteristics effecting adsorption differently based on differing system conditions.

Nano-adsorption performance has recently been related to the presence of specific crystal facets, namely high energy facets [9,25–31]. High energy facets are the termination faces of a well-defined crystal with higher surface energy and more dangling bonds, typically facets with Miller indices greater than one [31–33]. The best-studied examples of facet-dependent adsorption is the controlled synthesis of nanomaterials using preferentially adsorbed shape controllers to yield particles enriched for certain crystal facets [4,6,8,34,35]. For bulk scale adsorption behavior, theoretical and experimental evidence supports the importance of surface structure [5,17,28,29,31,36–39]. The CD-Music model, set forth by Heimstra et al., shows that only singly and triply coordinated surface oxygen groups of metal (hydr)oxides are reactive [40,41]. Congruently, Catalano et al., shows that selenite creates inner-sphere bidentate complexes with singly coordinated oxygen groups on the (1 0 0) of α-Fe_2O_3, while the doubly-coordinate oxygen groups are unreactive [42]. The density of reactive oxygen groups is believed to depend on surface geometries and surface sites, accounting for changes in adsorption capacities and mechanisms of adsorbates onto different hematite surfaces as well as onto the same surface of different adsorbents of similar structure such as α-Fe_2O_3 and Al_2O_3 [36,37].

(Hydr)oxide hydration studies further support the dependence of reactivity on the presence of singly and triply coordinated oxygen groups [37,43,44]. Since many adsorption reactions occur in aqueous systems, thermodynamically, the surface reactivity of hydrated metal (hydr)oxides more closely resembles actual surfaces than those of the pristine terminations. DFT modeling and experimental results show that the hydroxylated surfaces are more stable than dehydroxylated surfaces for adsorption [43,44]. Furthermore, it has been shown that different surface geometries and termination planes result in different densities of hydroxylated versus oxygen or iron terminated surfaces [37,43,44]. The influence of hydration may play an even larger role in dictating surface structure on the nano-scale than what is observed in the bulk studies [44].

For environmental purposes, elucidation of an SPF relationship for adsorption capacity and mechanism onto nanomaterials is paramount in designing improved remediation technologies. This study aims to elucidate relevant SPF relationships for the adsorption of selenium (Se) onto nα-Fe_2O_3. nα-Fe_2O_3 is an appropriate and relevant adsorbent due to the wide range of applications that can exploit its magnetic and electronic properties, as well as its reactive surface sites for adsorption and catalysis [45,46]. Furthermore, nα-Fe_2O_3 is well studied for inexpensive, diverse, controlled, and facile synthesis, and behaves similarly to other nano-metal oxides [31,33,34,47]. Finally, nano α-Fe_2O_3 is as an effective adsorbent for Se, and other similar oxyanions, in biomedical and environmental remediation scenarios [19].

Se is a model for other inorganic oxyanions with multiple oxidation states, that are more easily removed in the reduced state. It exists as an oxyanion with multiple forms, most notably, selenite (SeO_3^{2-}), and selenate (SeO_4^{2-}), which is more mobile, bioavailable and toxic than the reduced SeO_3^{2-} [48]. While Se is an essential micronutrient required at low concentrations [48], concentrations above 5 mg/kg-day are toxic to humans and 1.5 μg/L Se concentrations is of concern from an ecotoxicity perspective [49]. The US EPA has just lowered the aquatic life criteria for Se [49], yet no full scale technology exists that can remove Se to the desired concentrations in a cost effective and widely applicable manner [50].

The objective of this study is to evaluate the role of particle morphology on adsorption capacity and mechanism. Towards this goal, six different hematite nanoparticles were synthesized controlling for shape, size, and surface area without the use of capping agents. Adsorption capacity and binding environment of Se onto each of the particles was examined using *in situ* attenuated total reflectance-Fourier transform infrared (ATR-FTIR) spectroscopy and extended x-ray absorption fine structure (EXAFS) spectroscopy. Regression analysis was performed to determine the relevance and contribution of the different adsorbent properties on Se adsorption, a process that has previously been conducted for different organic adsorbates [51]. While this effort focuses on the extent to which different adsorbent properties enhance adsorption capacity for the specific system of nα-Fe_2O_3 and Se, future efforts can leverage this deep molecular understanding to ultimately inform design of more efficient and environmentally friendly nano-technology more broadly.

2. Materials and methods

2.1. Nanoparticle synthesis

All nα-Fe_2O_3 were synthesized using previously reported methods by: *Schwertmann and Cornell* method 1 (Particle B) [52], method 2 (Particle D) [52], method 3 (Particle C) [52], method 4 (Particle A) [52], and Sugimoto et al. (Particles E & F) [53] with ACS grade reagents. All nanoparticle suspensions were washed with DI water and centrifuged three times before dialysis (6000–8000 Dalton molecular weight cut off, Fisher Scientific) until conductance was below 5 μS. Final concentrations of nanoparticle suspensions were determined from inductively coupled plasma-mass spectrometry (ICP-MS; Perkin Elmer ICP-MS Elan DRC-e) analysis of suspensions dissolved in 10% trace metal grade HNO_3.

2.2. Nanoparticle characterization

Phase identification and crystal structure. Specific surface area (SSA) was determined using a 3-point N_2-physisorption Brunauer-Emmett-Teller (BET) isotherm after degassing for two hours at 200 °C (Particle Technology Laboratory). Synchrotron powder X-ray diffraction (SP-XRD) measurements where collected at the Canadian Light Source (CLS) Inc. CMCF-BM (08B1-1) beamline at an energy of 18 keV and a wavelength of 0.68888 Å. Data reduction and processing was performed as in Hamilton et al. [54]. All diffraction patterns were consistent with hematite phase iron-oxide (Fig. S1). *Size and Morphology.* Transmission electron micrographs (TEM) were obtained using a FEI Tecnai Osiris 200 kV transition electron microscope. Nanoparticle suspensions were placed on a lacy carbon grid supported with a 200 mesh copper holder (Ted Pella, Inc.) for TEM imaging. Crystal facet was determined with high resolution (HR) TEM (FEI TITAN 80–300). Scanning Electron Microscopy (SEM) was conducted on dilute suspensions of nα-Fe_2O_3 drop-coated onto silicon chips and imaged with a Hitachi SU8230 UHR Cold Field Emission (CFE) SEM. Dynamic Light Scattering (DLS) was completed using a ALV-GmbH instrument at an angle of 90°. The raw correlation functions were analyzed in MATLAB and Fortran, using the CONTIN Algorithm [19,55]. *Surface Properties.* Zeta potential and point of zero charge (PZC) of the nanoparticles were calculated from measured electrophoretic mobility measurements (Brookhaven Instruments ZetaPALS Zeta Potential Analyzer) after manually adjusting the pH of each nanoparticle slurry with HCl and NaOH.

2.3. Adsorption experiments

Adsorption experiments were completed with autoclaved DI in oxygen and carbon dioxide-free nitrogen environments in an InVivo 400 glovebox. Each of the starting Se solutions were adjusted to the desired pH ~ 3.5 ± 0.15 with 0.01 M HCl or NaOH and separated into 50-mL CORNING sterile polypropylene tube batch reactors. Adsorption experiments were completed at this low pH to ensure maximum adsorption of Se, limited variation in the protonation of Se oxyanions, and to minimize bound CO_2-species. Nano α-Fe_2O_3 particles were added to the suspensions such that the sorbate-sorbent ratio ranged from 0.21 at the start of the isotherm to 96 at the end of the isotherm. pH of the samples was monitored and adjusted after 12 h if necessary. Samples were reacted for 24 h (>17 h reported for system equilibrium) [19] to ensure steady-state was reached. Aliquots of each reactor were filtered through a 0.2 μm syringe-driven filter unit (PVDF Millipore) and acidified for ICP-MS analysis (Perkin Elmer ICP-MS Elan DRC-e). Experiments were completed in triplicate. Error is reported as standard propagated error.

2.4. EXAFS spectroscopy

Following adsorption experiments, reaction vessels were centrifuged, and decanted. The resulting paste was spread between Kapton tape, sealed, and frozen to preserve oxidation state and minimize contamination from CO_2. Se K-edge EXAFS spectroscopy was performed at the Hard X-ray Micro Analysis (HXMA) beamline 06ID-1 of the CLS in Saskatoon, Canada for Se(IV), whereas EXAFS for Se(VI) samples were measured at Beamline 20-BM (PNC-CAT) at the Advanced Light Source at Argonne National Labs. All samples were maintained at 20 K during measurements using a liquid helium flow cryostat. Athena and WinXAS3.2 were used for all data processing and analysis.

2.5. ATR-FTIR spectroscopy

ATR-FTIR spectroscopy was performed with a Burker Optics Equinox 55 FTIR spectrometer with $N_{2(l)}$-cooled MCT detector. Each nα-Fe_2O_3 suspension was coated onto a horizontal ZnSe crystal and Se solutions of increasing concentration and pH 3.5 ± 0.1 were added to the film for analysis. The Se solutions had a 0.01 M KCl background, to maintain constant ionic strength. Data were collected over 4000–400 cm^{-1} with 256 total scans at 8 cm^{-1} resolution. The background for each sample was the associated coated crystal and a 0.01 M KCl solution of pH 3.5 was used for water subtraction. The ATR-FTIR data were collected and processed using OPUS 5.5 (Bruker Optics Ltd., Ontario). The ATR-FTIR data was processed using a multivariate curve regression analysis on UNSCRAMBLER®-X (Camo software), to determine relevant bonding components.

2.6. Regression analysis

The effects of nα-Fe_2O_3 size, surface area and morphology on the adsorption capacity of $HSeO_3^-$ and SeO_4^{2-} were tested using multiple regression analysis, Eq. (1), in Stata [StataCorp LP, *Stata/MP 14.2 for Windows*]. Only particles for which frontier facet could be determined were included in the statistical analysis. All models that demonstrated collinearity were excluded and are discussed further in the supporting information (SI).

$$y = \propto + \beta_1 x_1 + \beta_2 x_2 + \cdots + \beta_n x_n + \varepsilon \quad (1)$$

The dependent variable is the mass normalized adsorption capacity, $q_i(\frac{\mu g}{g})$, for $HSeO_3^-$ or SeO_4^{2-}. $q_i(\frac{\mu g}{g})$ was calculated from Eq. (2) (discussed below) with parameters in Table 1 and Tables S4 for a given $C_e(\frac{\mu g}{L})$ value, randomly selected from a range of 10–10,000 $\frac{\mu g}{g}$. $x_1, x_2, \cdots, x_n$ are the *n* explanatory variables, including SSA, smallest dimension (SD), and frontier facet. The coefficients, β, describe the adsorption effects. α is the modeled constant and ε is the error term. All variables that demonstrated collinearity were excluded from the primary discussion but are described in the SI. Adjusted R^2 values were used to test the relative explanatory powers of different variables given the sample size.

3. Results

3.1. Characterization

Nano-hematite were synthesized in different sizes, shapes, and morphologies to determine how the different nano-properties influence Se adsorption. The sizes of the individual particles, characterized by the SD, range from 20 nm to just under 200 nm based on the SEM measurements (Fig. 1; Table 1). The most common aggregate size, as determined from DLS measurements, range from ~ 48 nm to 185 nm (Table 1; Fig. S6). The SSA measurements

Table 1
Characterization details for each of the synthesized particles.

Iron particle	SSA[a] (m^2/g)	Smallest dimension[b] (nm)	DLS mean (nm)	Frontier facet[c]	Crystallinity[d]
A	98.9 ± 0.1	18 ± 7	48	Unknown	Single
B	37.1 ± 0.8	23 ± 5	68	{1 1 0}	Single
C	25.13 ± 0.03	66 ± 8	50	Unknown	Poly
D	55.4 ± 0.2	150 ± 50	185	{1 1 0}	Poly
E	42.7 ± 0.4	160 ± 30	118	{0 1 2}	Poly
F	43.5 ± 0.2	190 ± 40	180	{0 1 2}	Poly

[a] Specific surface area (SSA) was determined by 3-point N_2 physisorption BET.
[b] Smallest dimension (SD), defined as the average of the smallest measured dimension, was determined from SEM.
[c] Frontier Facet is defined as the most prevalent external facet of the particle.
[d] Each particle was defined as single or polycrystalline based on TEM. More information provided in the SI.

range from 25 m^2/g to 98 m^2/g. While the upper bound of the SSA is 98.9 m^2/g for the smallest sized particle (A, SD = 18 nm), the lower bound of the SSA, 25.1 m^2/g, is for the third smallest sized particle (C, SD = 66 nm). The higher SSA for the larger particles could be attributed to increased surface roughness and polycrystallinity, as seen in Fig. 1.

Additional analyses were performed to determine particle crystal structure (Table 1). Particles A & B are single-crystalline (Fig. 1), while particles C-F are polycrystalline (Figs. S2 and S4C, D). Frontier facets, {0 1 2}, of Particles E & F were obtained from previously published reports by Sugitmoto et al. (Table 1) [53]. Particles B and D were indexed as {1 1 0} via SAED and HR-TEM images (Table 1; Figs. S3 and S4). Although, Particle D is polycrystalline, it consists of highly oriented sub-crystals with epitaxial growth on each substrate crystal (Fig. S4) allowing for frontier plane analysis. Unfortunately, despite being single-crystalline, the irregular shape of Particle A prohibits identification of the frontier plane.

3.2. Adsorption of selenite and selenate onto nα-Fe_2O_3

To test the influence of particle morphology on adsorption capacity, adsorption capacity must first be defined. Freundlich isotherms were used to quantify adsorption capacity for all the particles in a consistent manner due to the empirical nature and appropriateness of the heterogeneity assumptions associated with the model. The linear form of the Freundlich adsorption isotherms (Eq. (2)) for selenite (hydrogenselenite, $HSeO_3^-$, dominates at pH 3.5) and selenate (SeO_4^{2-}) for each of the synthesized particles (A-F) are shown in Fig. 2 with parameters in Table 2 and further presented in the SI.

$$q = K_f C_e^{\frac{1}{n}} \quad (2)$$

Here, q is the sorption capacity and C_e is the equilibrium selenium concentration as discussed above. K_f is the Freundlich capacity parameter in units of $\left[\left(\frac{mg}{g}\right)\left(\frac{L}{mg}\right)^{\frac{1}{n}}\right]$ for mass normalized sorptivities ($K_{f(M)}$) and units of $\left[\left(\frac{mg}{m^2}\right)\left(\frac{L}{mg}\right)^{\frac{1}{n}}\right]$ for surface area normalized sorptivities ($K_{f(SA)}$), and n (dimensionless) is the intensity parameter. [48,49]

Therefore, in addition to adsorption capacities themselves, the isotherms provide insight to what influences those capacities. If surface area (SA), for which SSA is a proxy, and size are the only determinants for sorption capacity, then, one would expect the relative ranking of $K_{f(M)}$ for particle sets A through F to be the same for both $HSeO_3^-$ and SeO_4^{2-}. This is not observed (Fig. 2A and B). Instead, Fig. 2A and B demonstrate that the different sorbents have different adsorption capacities for $HSeO_3^-$ versus SeO_4^{2-}. Furthermore, if the surfaces of the synthesized nanoparticles of the same material (e.g., α-Fe_2O_3) have similar adsorption affinities/adsorption sites, $K_{f(SA)}$ for all particles would be equal for each adsorbate. However, $K_{f(SA)}$ values are not equivalent for the different particles, nor is the $K_{f(SA)}$ magnitude consistent between Se complexes (Fig. 2C and D; Table 2). Therefore, SSA is not the primary determinant of Se sorption on nα-Fe_2O_3, as is largely held in sorption literature [16] and some other sorbent descriptor is influencing the sorption

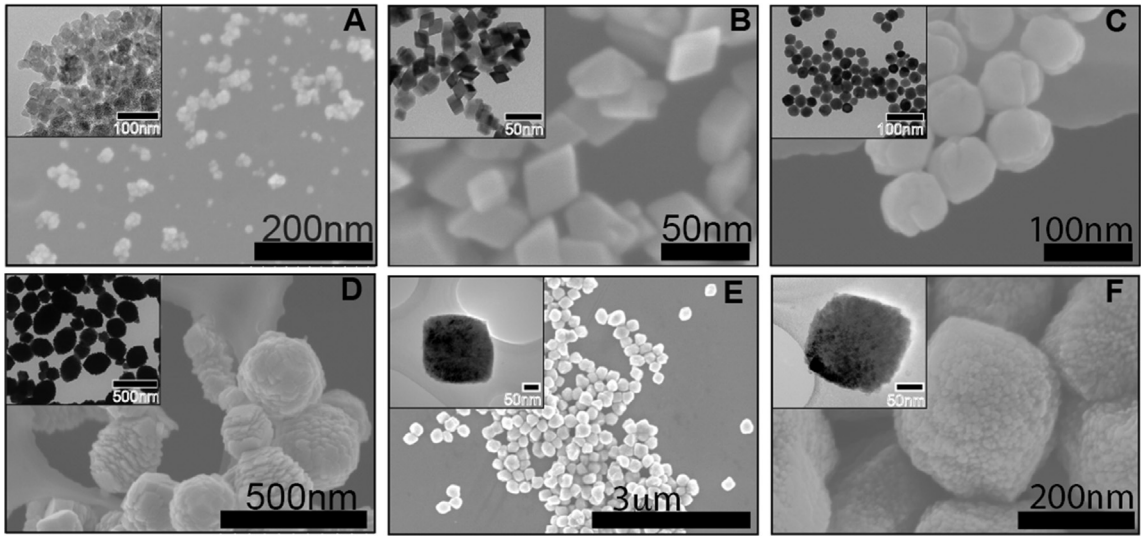

Fig. 1. SEM and TEM images. The particles are labeled A through F, smallest to largest respectively based on smallest measured dimension.

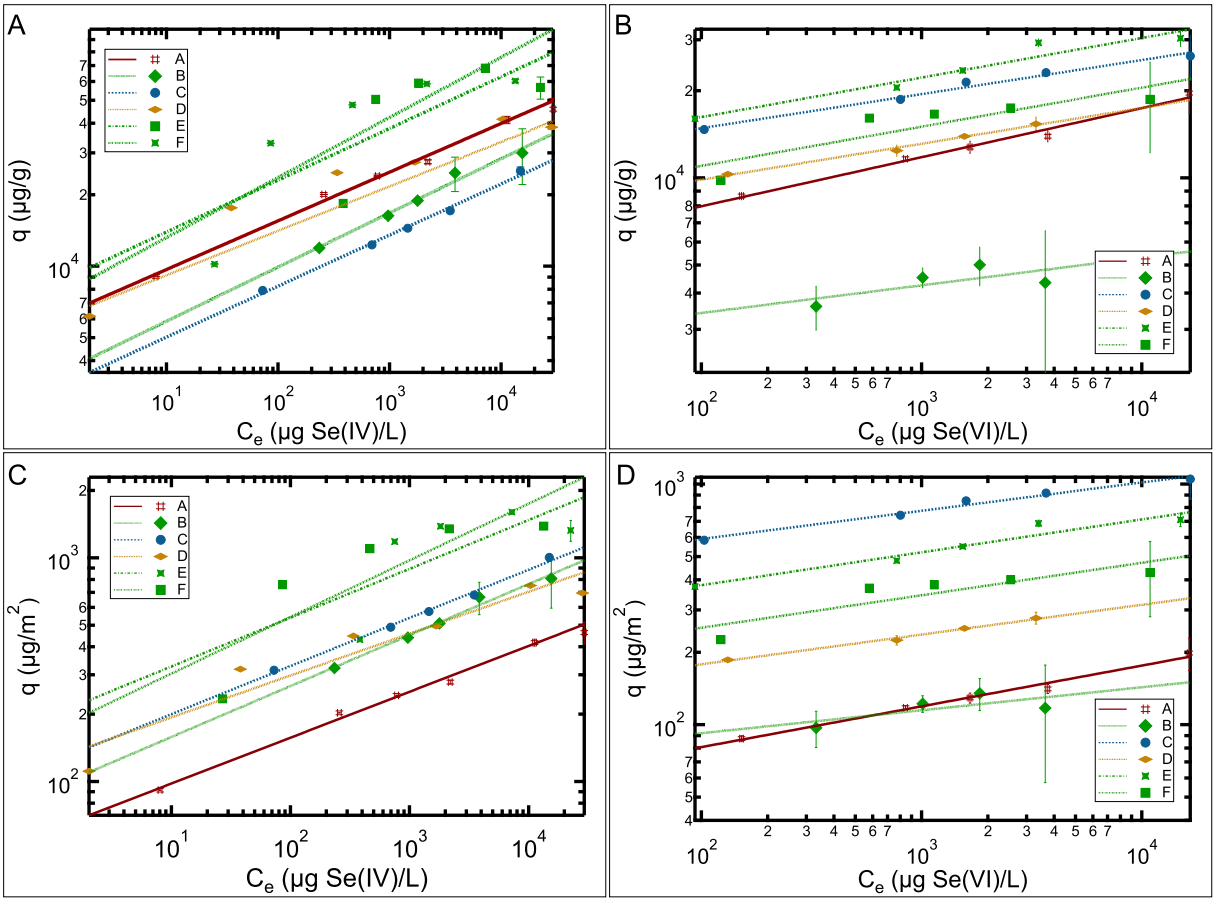

Fig. 2. Freundlich Isotherms. Freundlich isotherms represented on a log-log scale for adsorption of $HSeO_3^-$ (A) and SeO_4^{2-} (B) mass normalized and $HSeO_3^-$ (C) and SeO_4^{2-} (D) surface area normalized. All isotherms were conducted at T = 25 °C, pH 3.5 ± 0.1, and I = 0.01 M KCl for 24hrs. pH was adjusted after 12 h. Error is presented as standard error. Particles are listed in order of smallest to largest. Freundlich parameters are provided in Table 2. The colors are based on relative surface area with red as the largest and blue as the smallest. (For interpretation of the references to colour in this figure legend, the reader is referred to the web version of this article.)

Table 2
Freundlich isotherm fit parameters for Se(IV) and Se(VI).

Iron particle	$K_{f(M)}$						$K_{f(SA)}$					
	$HSeO_3^-$			SeO_4^{2-}			$HSeO_3^-$			SeO_4^{2-}		
	K	1/n	r^2	K	1/n	r^2	K	1/n	r^2	K	1/n	r^2
A	6000 ± 1	0.20 ± 0.01	0.99	3700 ± 1	0.17 ± 0.01	0.99	61 ± 1	0.19 ± 0.01	0.99	37 ± 1	0.17 ± 0.01	0.986
B	3500 ± 1	0.23 ± 0.02	0.98	2200 ± 2	0.10 ± 0.07	0.5	94 ± 1	0.22 ± 0.02	0.98	59 ± 34	0.08 ± 0.07	0.495
C	3100 ± 1	0.22 ± 0.01	0.99	8600 ± 1	0.12 ± 0.01	0.98	120 ± 1	0.22 ± 0.01	0.99	340 ± 1	0.12 ± 0.01	0.984
D	7000 ± 1	0.19 ± 0.03	0.92	5600 ± 1	0.12 ± 0.01	0.99	130 ± 1	0.19 ± 0.03	0.92	100 ± 1	0.12 ± 0.01	0.992
E	8400 ± 3	0.22 ± 0.10	0.47	8600 ± 1	0.14 ± 0.02	0.94	200 ± 3	0.22 ± 0.10	0.47	200 ± 1	0.14 ± 0.02	0.938
F	7400 ± 2	0.25 ± 0.09	0.72	5900 ± 1	0.13 ± 0.04	0.78	170 ± 2	0.25 ± 0.09	0.72	140 ± 1	0.13 ± 0.04	0.777

K describes adsorption capacity of the nα-Fe_2O_3, 1/n is directly related to the mean site energy and the energy of adsorption, r^2 is the statistical goodness of fit parameter of the log-log linearized Freundlich isotherm and the corresponding data. A description of the Freundlich modeling is provided in the SI.

capacity of the nα-Fe_2O_3. Specifically, the surfaces of the different particles must contain different number of available adsorption sites and/or binding energies to manifest variable $K_{f(SA)}$ between particles of the same underlying chemical composition.

3.3. Mechanisms of Se adsorption onto α-Fe_2O_3 from EXAFS and in-situ ATR-FTIR

Adsorption behavior is defined by both the adsorption capacities as well as by the mechanism through which adsorption occurs. EXAFS and *in-situ* ATR-FTIR spectroscopy were used to probe the surfaces of the nα-Fe_2O_3 with adsorbed $HSeO_3^-$ and SeO_4^{2-} (Figs. 3 and 4) to inform how the different particles impacted Se adsorption mechanisms. While there have been several spectroscopic studies of selenite oxyanion onto iron and aluminum (hydr)oxides, this is the first to assess how different morphologies impact the binding environment [42,56–58]. The Fourier transformed EXAFS spectra demonstrate an Se—O scattering path with a coordination number of three and radial distance around 1.69 Å and a second shell for the Se—Fe scattering with a coordination number of two and a radial distance around 3.04 Å. These fit parameters (Fig. 3a, Table S3) indicate that $HSeO_3^-$ forms *inner-sphere* bidentate binuclear corner sharing complexes with nα-Fe_2O_3, in agreement with previous findings for selenite complexes on iron oxides [58–60].

The Fourier transformed data exhibits a shoulder in the second shell at a radial distance (R) of ~2.57 Å; Manceau et al. attributed a similar shoulder in their Fourier transformed spectra for selenite adsorbed onto the amorphous hydrous ferric oxide (HFO) at R ≅ 2.60 Å (without phase correction) to a percentage of edge sharing bidentate mononuclear complexes complexes [58]. The variance in the radial distances between this work and that of Manceau et al., may be attributed to the different crystal structure packing of α-Fe_2O_3 compared to HFO [58]. The relative size of this shoulder is dependent on the proportion of available edge versus corner sharing sites on the iron oxide surface. This proportion is directly related to the surface structure of the particle and the associated bonding sites [58]. Therefore, the variation in the shoulder formation in our EXAFS data between the particles can be attributed to a difference in the relative number of the two unique bonding sites (edge vs corner) on the surface of the different particles (A-F).

Conversely, SeO_4^{2-} sorption onto nα-Fe_2O_3 appears to be dominated by *outer-sphere* complexes (Fig. 3b) with a minor contribution from inner-sphere complexation. Se—O scattering fit with a coordination of four oxygens with R = 1.65 Å and the appearance of a small second shell fit with a coordination of two near R = 3.37–3.39 Å for the Se—Fe scattering path. (The only exception is for particle A, which shows no evidence of a second shell). With these distances, one can assume an inner-sphere bidentate complex [22]. The slight variation in R as compared to other literature reports can be attributed to the use of nanomaterials rather than bulk material, or to the shift from goethite to hematite [59]. The EXAFS results are consistent with previous reports of combined inner-sphere and outer-sphere complexes associated with selenate adsorption on iron oxides [19,56,61]. There is, however, a slight discrepancy between this data and that previously reported for SeO_4^{2-} oxyanion adsorption onto α-Fe_2O_3 and other iron oxy (hydr-) oxides, by others [58,59,61]. For example, Peak and Sparks reported primarily inner-sphere complexation on nα-Fe_2O_3 by SeO_4^{2-} at pH 3.5 [59]; however, this is attributed to their use of a higher background ionic strength, since the relative percentage of inner-sphere complexes increases with ionic strength. As is seen below, this discrepancy may also be associated with the structures of the nα-Fe_2O_3 studied.

ATR-FTIR was used to more effectively explore the relationship between inner and outer-sphere complexes of SeO_4^{2-}. The ATR-FTIR sorption data for each of the particles is presented in the SI (Fig. S7). Free SeO_4^{2-} has tetrahedral symmetry (T_d) with a single peak at 872 cm^{-1} with a triply degenerate stretch at Se—O (υ_3) [19]. When SeO_4^{2-} complexes, it results in the splitting of this asymmetric υ_3 stretch into two or three peaks for non-protonated mono- or bidentate complexes respectively [19]. For a mono-dentate complex, T_d becomes C_{3v} with υ_3 splitting into two peaks located at ca. 880 cm^{-1} and 850 cm^{-1} and a υ_1 stretch at 820 cm^{-1} [59]. This data demonstrated peak splits at ~ 879 cm^{-1} 844 cm^{-1} and 825 cm^{-1}. Additionally, there is evidence of the outer-sphere stretch at 872 cm^{-1}. This is in agreement with what has been previously published and suggestive of a combination of inner- and outer-sphere complexes [19,59]. Johnston et al. demonstrates data similar to the ATR-FTIR results presented here (Figs. S7 and S8) [61]; however, it appears that Johnston's [62] fourth peak at 910 cm^{-1} starts to dissipate with decreasing pH suggesting a protonated or strongly coordinated H-bonded monodentate system [61,63]. Therefore, based upon their peak assignment, it is expected that the 910 cm^{-1} Se—O vibration would be absent at the pH of our measurements.

A multivariate curve regression (MCR) analysis was completed and is presented here to better describe the inner and outer-sphere relationships. According to the MCR analysis (Fig. 4), all of the nα-Fe_2O_3 particles demonstrate two components, indicating the presence of both inner-sphere and outer-sphere complexes as identified by the location and shape of the primary spectra (Fig. S7). Particles A, B, C, E, & F (Fig. 4A, B, C, E, & F) are primarily

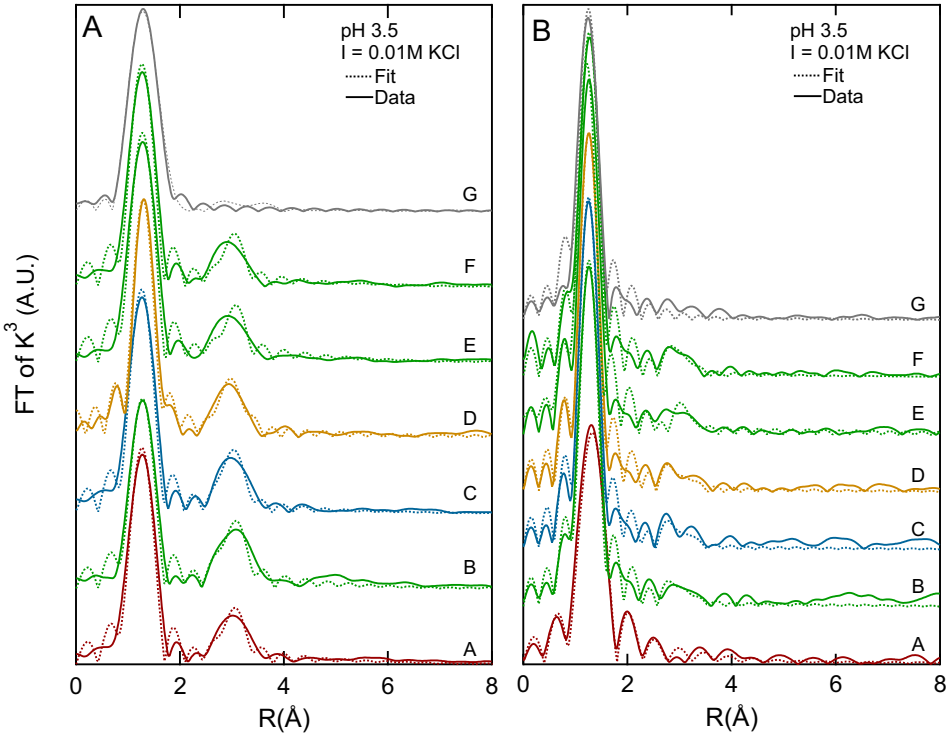

Fig. 3. Se K-edge EXAFS. Se edge EXAFS of $HSeO_3^-$ (A) and SeO_4^{2-} (B) bound onto the different synthesized hematite nanoparticles. $HSeO_3^-$ is bound primarily via inner-sphere bidentate binuclear complexes, whereas SeO_4^{2-} forms primarily outer-sphere complexes with some evidence of inner-sphere complexation. The modeled data is represented by the dotted line whereas the solid line is the processed EXAFS data. Colors indicate relative surface area with red as the largest and blue as the smallest. Grey spectra are the corresponding reference spectra. (For interpretation of the references to colour in this figure legend, the reader is referred to the web version of this article.)

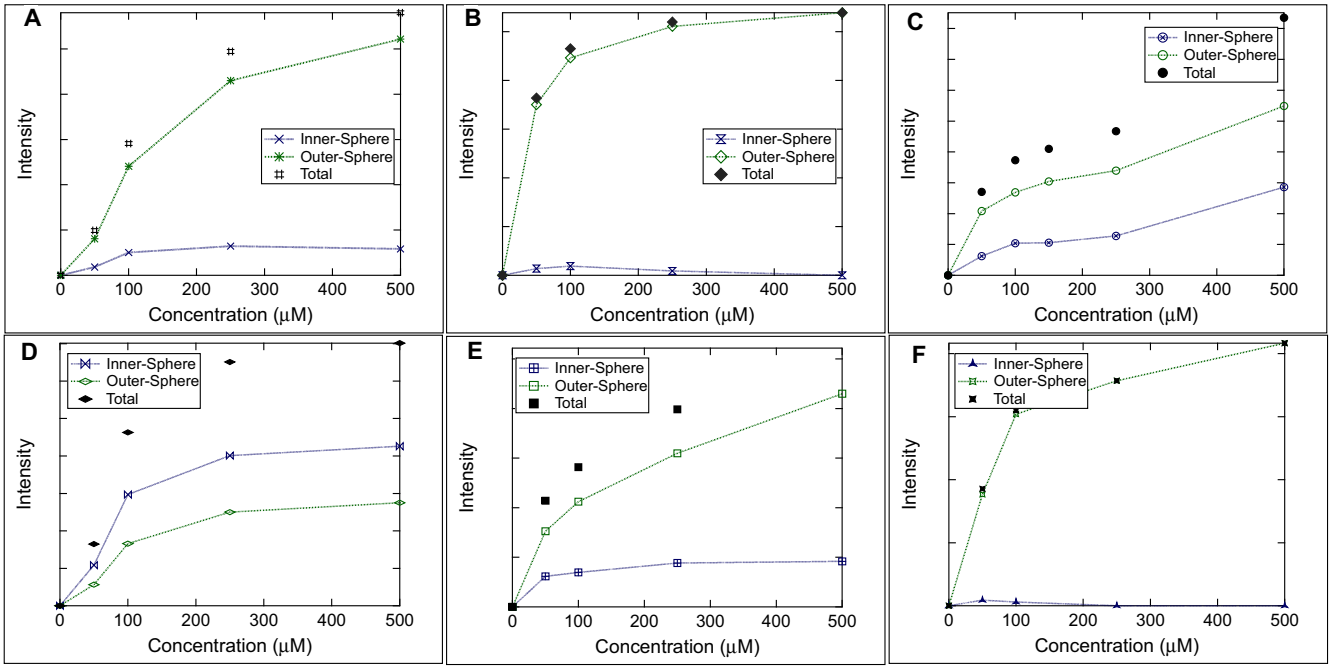

Fig. 4. Multicomponent regression (MCR) analysis of *in-situ* ATR-FTIR from SeO_4^{2-} bound to nano-hematite. The MCR analysis suggests that the percentage of inner-sphere complex of SeO_4^{2-} with hematite nano-particles changes with Se concentration and with the different particle types.

outer-sphere complexes with a smaller percentage of inner-sphere formation across the concentration range. Particle D (Fig. 4D) has more inner-sphere complexes than outer-sphere across the concentration range. While this is not associated with higher K_f (regardless of normalization), it has implications for sorption mechanism. More generally, a combination of inner and outer-sphere complexes appears to offer the highest K_f values for SeO_4^{2-}. This relationship implies that some intrinsic property of $HSeO_3^-$ and the SeO_4^{2-} in relation to nα-Fe_2O_3 creates preferences for not only inner-sphere and outer-sphere complexes, respectively, but also the type of inner-sphere complexes that are formed.

In general, the proportion of outer-sphere complexes increases with increasing SeO_4^{2-} concentration, suggesting that sites available for the energetically more favorable inner-sphere complexes reach a saturation point after which, only outer-sphere complex sites are available. As mentioned previously, while other reports have found that SeO_4^{2-} forms a combination of inner- and outer-sphere complexes with iron oxides [19,56,61], the proportion of complex type was attributed to system pH, background salt concentrations [56], and iron structure [19,61]. In fact, while Peak and Sparks observed an effect on adsorption mechanism with SO_4^{2-} onto goethite [64], they found no evidence of Se loading impacting adsorption mechanism onto goethite [59]. Therefore, this is the first evidence that Se loading also impacts the bonding environment.

4. Discussion

The data suggests that SSA and size alone do not determine nα-Fe_2O_3 sorption capacity of Se oxyanions; therefore, multivariate regression analyses were conducted to elucidate which nα-Fe_2O_3 characteristics are significant determinants of Se oxyanion sorption capacity. This approach is similar to that used for small organic sorbents, but in this instance, sorbent descriptors are utilized rather than the molecular sorbate descriptors previously reported [51]. Additionally, data is tabulated to explicate relationships between bonding environment and facet.

The statistical findings (Table 3) demonstrate the importance of crystal surface structure in adsorption of Se onto nα-Fe_2O_3 in

Table 3
Multilinear Regression analysis relating nα-Fe_2O_3 characteristics to Se adsorption.

Variable[a]	Model 1		Model 2		Model 3		Model 4	
	B	SE[b]	B	SE[b]	B	SE[b]	B	SE[b]
$HSeO_3^-$								
SSA	−0.661***	0.100***	−1.55***	0.078***	–	–	0.793***	0.085***
SD	–	–	0.483***	0.020***	–	–	–	–
Facet	–	–	–	–	−0.526***	0.021***	−0.678***	0.318***
Constant	13.1***	0.388***	14.1***	0.269***	10.8***	0.016***	7.87***	0.318***
R^{2c}	0.0762		0.5667		0.5477		0.6129	
SeO_4^{2-}								
SSA	0.253	0.146	−1.29***	0.077***	–	–	2.86***	0.0647***
SD	–	–	0.852***	0.020***	–	–	–	–
Facet	–	–	–	–	−0.666***	0.032***	−1.22***	0.019***
Constant	8.77***	0.565***	10.6***	0.268***	10.1***	0.024***	−0.620*	0.243*
R^{2c}	0.0039		0.7822		0.4476		0.8804	

[a] nα-Fe_2O_3 characteristics were treated as either continuous variables that are natural log transformed or as categorical variables and are further discussion in the SI.
[b] B and SE comprise the β values in Eq. (1).
[c] Adjusted R^2-value is presented *p < 0.05, **p < 0.01, ***p < 0.001.

general and also for each Se species individually. When describing adsorption of either $HSeO_3^-$ and SeO_4^{2-}, the explanation of the variance (R^2) increases when facet is included in the analysis over inclusion of only size or SSA (Table 3). The analysis shows $HSeO_3^-$ adsorption capacity is higher when there is less {1 1 0} over {0 1 2} frontier surface. Additionally, based on the facet β coefficient, for the same increase in amount of {1 1 0} surface there is a greater decrease in SeO_4^{2-} adsorption capacity than in $HSeO_3^-$ sorption capacity. These results agree with previous findings from studies on oxyanion adsorption onto α-Fe_2O_3 [24,65]. Sugimoto and Wang [65] attribute increased adsorption of SO_4^{2-} (similar in structure to SeO_4^{2-}) onto α-Fe_2O_3 to the presence of the more reactive {0 1 2} facets [65]. Further, Huang et al. [24] conclude that the formation of bidentate binuclear complexes of $HCrO_4^-$ onto the {1 1 0} facet of nα-Fe_2O_3, the same complexation type indicated by the above spectroscopy for $HSeO_3^-$, led to preferential adsorption over the {0 0 1} facet. The regression analysis results support the hypothesis that crystal surface structure of nα-Fe_2O_3 is a more significant contributor to adsorption capacity than particle size or surface area. This further confirms Torrent et al.'s [17] conclusions where the authors attribute enhanced adsorption capacity of phosphate onto goethite surfaces, to the different exposed facets [17]. Although the preferred facets are different between this study and that one differ, this is likely due to the different sorbate/sorbent systems examined in each study.

The presence of an edge sharing complex over a corner sharing complex presents itself in the raw EXAFS data (Fig. 3) as a shorter radial distance of the second shell. As mentioned previously, the relative size of this shoulder depends on the proportion of one complex over the other. Therefore, the intensity of each radial distance of the second shell was used to compare frontier facet with $HSeO_3^-$ inner-sphere complexation type (Table 4). The resulting data strongly indicates more corner sharing (binuclear) complexes (longer bond distances) on the {1 1 0} facet and more edge sharing (mononuclear) complexes (shorter bond distances) on the {0 1 2} facet (Fig. 5), in agreement with Huang et al. and Catalano et al. [24,42]. These findings also support Catalano et al.'s [42] thesis that $HSeO_3^-$ binds with the singly coordinated oxygen groups since the {0 1 2} and {1 1 0} facets of α-Fe_2O_3 has a greater density of singly and triply coordinated surface sites as compared to other facets, in agreement with Hiemstra et al. [40,41]. The results also suggest increased adsorption of inner-sphere complexing oxyanions on facets where there is the formation of monodentate binuclear complexes. The results further suggest, based on Huang et al.'s [24] findings, that binuclear complexes may results in greater adsorption capacity than mononuclear complexes. This analysis demonstrates how the presence of different proportions of surface sites can impact adsorption behavior despite similarities in surface area [19], since different facets have different proportions of available surface sites, as was suggested by Lounsbury et al. previously

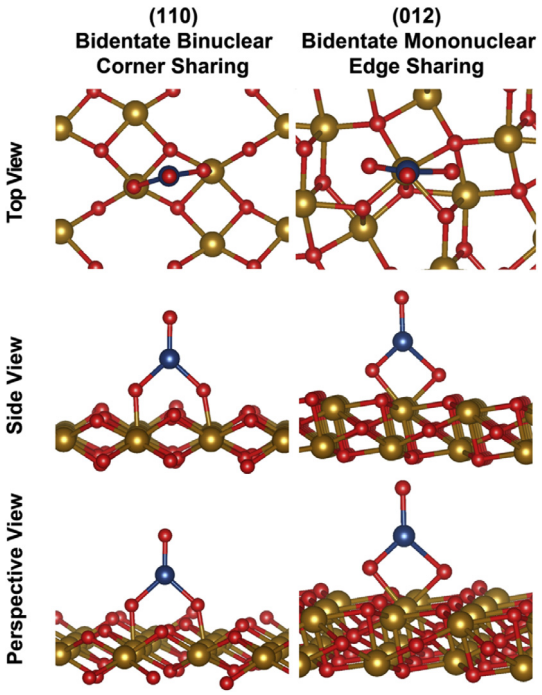

Fig. 5. *Inner-sphere Bonding of Selenium on Hematite Facets Schematic.* $HSeO_3^-$ forms bidentate binuclear corner sharing complexes on the {1 1 0} facet of nano-hematite and bidentate mononuclear edge sharing complexes with the {0 1 2} facet of nano-hematite (B).

[19,33]. The presence of these surface sites thus dictate bonding behavior. Overall, these results further support the premise that adsorption mechanism is dependent on nanomaterial surface structure in addition to surface area or size.

5. Conclusion

This is the first study to assess how nα-Fe_2O_3 morphology effects adsorption behavior of Se, and the first that examines morphology in combination with size and surface area for nano-adsorbents. Comprehensive analysis of nα-Fe_2O_3 particles and Se adsorption behavior onto the particles demonstrates the importance of crystal morphology on adsorption capacity and adsorption mechanism. Specifically, the data indicates that {0 1 2} facets promote adsorption of SeO_4^{2-} and $HSeO_3^-$ over {1 1 0} facets with absence of the {1 1 0} facet having a greater effect on SeO_4^{2-} adsorption than that of $HSeO_3^-$. {1 1 0} and {0 1 2} facets bind $HSeO_3^-$ via inner-sphere complexes, albeit {1 1 0} binds bidentate binuclear complexes, while {0 1 2} binds via bidentate mononuclear complexes. SeO_4^{2-} binds to nano-hematite primarily

Table 4
Tabulated data comparing nα-Fe_2O_3 facets to bonding behavior of $HSeO_3$.

Facet	Radial distance relative intensity							
	Corner sharing				edge sharing			
	Less		More		Less		More	
	1[a]	2[a]	3[a]	4[a]	1[a]	2[a]	3[a]	4[a]
{0 1 2}	X[b]	X[b]	0	0	0	0	X[b]	X[b]
{1 1 0}	0	0	X[b]	X[b]	X[b]	X[b]	0	0

[a] Place holders for the radial distance value from the EXAFS data, 1 corresponds to the shortest radial distance and corner sharing complexes whereas 4 corresponds to the longest radial distance and edge sharing complexes.
[b] X is used to show that the {0 1 2} facet has shorter radial distances that correspond to corner sharing complexes whereas the {1 1 0} facet has longer radial distances that correspond to edge sharing complexes.

through outer-sphere complexes with some proportion of inner-sphere complex dependent on the specific facet. The findings of this study support the hypothesis that adsorption capacity and mechanism of nα-Fe_2O_3, and likely nano-metal oxides more generally, are contingent upon and determined by the individual facets and further contingent on surface sites since different facets have different proportions of available surface sites [33]. These results are in agreement with literature examining similar adsorbate systems [17,24,42,65]. Overall, these results offer additional design targets, under the SPF-SPH framework, for future synthesis of more efficient and effective nano adsorbents, especially in environmentally relevant systems and further have implications in designing adsorbents tuned for specific environments, such as creation of a more selective adsorbents. These results encourage adsorption research to focus on surface crystallography, an understudied aspect of nanosorbent processes, which may help to explain reported disparities in adsorption behavior observed for the same combinations of sorbate-nanosorbent systems.

Acknowledgements

Many thanks to Dr. Sara Hashmi for her help in collecting and analyzing the point of zero charge data, David Hilger for his help in collecting PS-XRD data, Riley Coulthard for taking a few shifts at the CLS, all the staff who helped at beamlines and in analytics. Research described in this work was performed at the Canadian Light Source, which is supported by the Natural Sciences and Engineering Research Council of Canada, the National Research Council Canada, the Canadian Institutes of Health Research, the Province of Saskatchewan, Western Economic Diversification Canada, and the University of Saskatchewan. This research used resources of the Advanced Photon Source, a U.S. Department of Energy (DOE) Office of Science User Facility operated for the DOE Office of Science by Argonne National Laboratory under Contract No. DE-AC02-06CH11357. This work was supported by the NSF Nanosystems Engineering Research Center for Nanotechnology-Enabled Water Treatment (ERC-1449500). This research was also funded by an Environmental Protection Agency Science to Achieve Results fellowship. Additional acknowledgement to Brad Erkkila and Jonas Karosas at the Yale Analytical and Stable Isotope Center, and Mike Rookes at the Yale Institute for Nanoscience and Quantum Engineering.

Appendix A. Supplementary material

Supplementary data to this article can be found online at https://doi.org/10.1016/j.jcis.2018.11.018.

References

[1] M.C. Roco, C.A. Mirkin, M.C. Hersam, Nanotechnology research directions for societal needs in 2020: summary of international study, J. Nanoparticle Res. 13 (3) (2011) 897–919.
[2] M.F. Ashby, P.J. Ferreira, D.L. Schodek, Chapter 9 - design environments and systems, in: Nanomaterials, Nanotechnologies and Design, Butterworth-Heinemann, Boston, 2009, pp. 291–402.
[3] L.M. Gilbertson, J.B. Zimmerman, D.L. Plata, J.E. Hutchison, P.T. Anastas, Designing nanomaterials to maximize performance and minimize undesirable implications guided by the Principles of Green Chemistry, Chem. Soc. Rev. 44 (16) (2015) 5758–5777.
[4] V.F. Puntes, K.M. Krishnan, A.P. Alivisatos, Colloidal nanocrystal shape and size control: the case of cobalt, Science 291 (5511) (2001) 2115–2117.
[5] X.M. Zhou, J.Y. Lan, G. Liu, K. Deng, Y.L. Yang, G.J. Nie, J.G. Yu, L.J. Zhi, Facet-mediated photodegradation of organic dye over hematite architectures by visible light, Angew. Chem. Int. Ed. 51 (1) (2012) 178–182.
[6] C.Y. Chiu, Y.J. Li, L.Y. Ruan, X.C. Ye, C.B. Murray, Y. Huang, Platinum nanocrystals selectively shaped using facet-specific peptide sequences, Nat. Chem. 3 (5) (2011) 393–399.
[7] A.M. Bond, Modern Polarographic Methods in Analytical Chemistry, vol. 4, CRC Press, 1980.
[8] C.J. Murphy, Nanocubes and nanoboxes, Science 5601 (2002, 298,) 2139-+.
[9] X. Mou, X. Wei, Y. Li, W. Shen, Tuning crystal-phase and shape of Fe_2O_3 nanoparticles for catalytic applications, CrystEngComm 14 (16) (2012) 5107–5120.
[10] C. Lemire, R. Meyer, S. Shaikhutdinov, H.J. Freund, Do quantum size effects control CO adsorption on gold nanoparticles?, Angew Chem. Int. Ed. Engl. 43 (1) (2004) 118–121.
[11] Y. Yang, H.X. Ma, J. Zhuang, X. Wang, Morphology-controlled synthesis of hematite nanocrystals and their facet effects on gas-sensing properties, Inorg. Chem. 50 (20) (2011) 10143–10151.
[12] A.K. Gupta, M. Gupta, Synthesis and surface engineering of iron oxide nanoparticles for biomedical applications, Biomaterials 26 (18) (2005) 3995–4021.
[13] X.L. Qu, P.J.J. Alvarez, Q.L. Li, Applications of nanotechnology in water and wastewater treatment, Water Res. 47 (12) (2013) 3931–3946.
[14] M. Hua, S. Zhang, B. Pan, W. Zhang, L. Lv, Q. Zhang, Heavy metal removal from water/wastewater by nanosized metal oxides: a review, J. Hazard. Mater. 211 (2012) 317–331.
[15] X. Wei, S. Bhojappa, L.-S. Lin, R.C. Viadero Jr, Performance of nano-magnetite for removal of selenium from aqueous solutions, Environ. Eng. Sci. 29 (6) (2012) 526–532.
[16] F. Maurin, J. Rouquero, K.S.W. Sing, P. Llewellyn, Adsorption by Powders and Porous Solids: Principles, Methodology and Applications, second ed., Elsevier, 2014.
[17] J. Torrent, V. Barron, U. Schwertmann, Phosphate adsorption and desorption by goethites differing in crystal morphology, Soil Sci. Soc. Am. J. 54 (4) (1990) 1007–1012.
[18] T. Tuutijarvi, R. Vahala, M. Sillanpaa, G. Chen, Maghemite nanoparticles for As (V) removal: desorption characteristics and adsorbent recovery, Environ. Technol. 33 (16) (2012) 1927–1936.
[19] A.W. Lounsbury, J.S. Yamani, C.P. Johnston, P. Larese-Casanova, J.B. Zimmerman, The role of counter ions in nano-hematite synthesis: implications for surface area and selenium adsorption capacity, J. Hazard. Mater. 310 (2016) 117–124.
[20] S. Goldberg, I. Lebron, D.L. Suarez, Z.R. Hinedi, Surface characterization of amorphous aluminum oxides, Soil Sci. Soc. Am. J. 65 (1) (2001) 78–86.
[21] L.S. Balistrieri, T.T. Chao, Selenium adsorption by goethite, Soil Sci. Soc. Am. J. 51 (5) (1987) 1145–1151.
[22] K.F. Hayes, C. Papelis, J.O. Leckie, Modeling ionic-strength effects on anion adsorption at hydrous oxide solution interfaces, J. Colloid Interf. Sci. 125 (2) (1988) 717–726.
[23] A.S. Madden, M.F. Hochella Jr., T.P. Luxton, Insights for size-dependent reactivity of hematite nanomineral surfaces through Cu^{2+} sorption, Geochim. Cosmochim. Acta 70 (16) (2006) 4095–4104.
[24] X.P. Huang, X.J. Hou, F.H. Song, J.C. Zhao, L.Z. Zhang, Facet-dependent Cr(VI) adsorption of hematite nanocrystals, Environ. Sci. Technol. 50 (4) (2016) 1964–1972.
[25] L. Zhang, W.X. Niu, G.B. Xu, Synthesis and applications of noble metal nanocrystals with high-energy facets, Nano Today 7 (6) (2012) 586–605.
[26] E.S. Jang, J.H. Won, S.J. Hwang, J.H. Choy, Fine tuning of the face orientation of ZnO crystals to optimize their photocatalytic activity, Adv. Mater. 18 (24) (2006) 3309-+.
[27] N. Tian, Z.Y. Zhou, S.G. Sun, Y. Ding, Z.L. Wang, Synthesis of tetrahexahedral platinum nanocrystals with high-index facets and high electro-oxidation activity, Science 316 (5825) (2007) 732–735.
[28] A. Matsuda, H. Mori, Theoretical study on crystal-facet dependency of hydrogen storage rate for shape controlled Pd nano particles, Chem. Phys. Lett. 644 (2016) 255–260.
[29] G. Li, H. Kobayashi, S. Dekura, R. Ikeda, Y. Kubota, K. Kato, M. Takata, T. Yamamoto, S. Matsumura, H. Kitagawa, Shape-dependent hydrogen-storage properties in pd nanocrystals: which does hydrogen prefer, octahedron (1 1 1) or Cube (1 0 0)?, J Am. Chem. Soc. 136 (29) (2014) 10222–10225.
[30] X.G. Han, M.S. Jin, S.F. Xie, Q. Kuang, Z.Y. Jiang, Y.Q. Jiang, Z.X. Xie, L.S. Zheng, Synthesis of tin dioxide octahedral nanoparticles with exposed high-energy 221 facets and enhanced gas-sensing properties, Angew. Chem. Int. Ed. 48 (48) (2009) 9180–9183.
[31] J.J. Ouyang, J. Pei, Q. Kuang, Z.X. Xie, L.S. Zheng, Supersaturation-controlled shape evolution of alpha-Fe_2O_3 nanocrystals and their facet-dependent catalytic and sensing properties, ACS Appl. Mater. Interf. 6 (15) (2014) 12505–12514.
[32] C. Kitel, Introduction to solid state physics, 1971.
[33] R.M. Cornell, U. Schwertmann, The Iron Oxides: Structure, Properties, Reactions, Occurrences and Uses, second ed., Wiley-VCH, Weinheim, 2003.
[34] B.L. Lv, Z.Y. Liu, H. Tian, Y. Xu, D. Wu, Y.H. Sun, Single-crystalline dodecahedral and octodecahedral alpha-Fe_2O_3 particles synthesized by a fluoride anion-assisted hydrothermal method, Adv. Funct. Mater. 20 (22) (2010) 3987–3996.
[35] A.P. Alivisatos, Semiconductor clusters, nanocrystals, and quantum dots, Science 271 (5251) (1996) 933–937.
[36] J.R. Bargar, T.P. Trainor, J.P. Fitts, S.A. Chambers, G.E. Brown, In situ grazing-incidence extended X-ray absorption fine structure study of Pb(II) chemisorption on hematite (0 0 0 1) and (1 −1 0 2) surfaces, Langmuir 20 (5) (2004) 1667–1673.
[37] S.E. Mason, C.R. Iceman, K.S. Tanwar, T.P. Trainor, A.M. Chaka, Pb(II) adsorption on isostructural hydrated alumina and hematite (0 0 0 1) surfaces: a DFT study, J. Phys. Chem. C 113 (6) (2009) 2159–2170.
[38] J.X. Wang, H. Inada, L. Wu, Y. Zhu, Y. Choi, P. Liu, W.-P. Zhou, R.R. Adzic, Oxygen reduction on well-defined core–shell nanocatalysts: particle size, facet, and Pt shell thickness effects, J. Am. Chem. Soc. 131 (47) (2009) 17298–17302.

[39] J.M. Pettibone, D.M. Cwiertny, M. Scherer, V.H. Grassian, Adsorption of organic acids on TiO_2 nanoparticles: effects of pH, nanoparticle size, and nanoparticle aggregation, Langmuir 24 (13) (2008) 6659–6667.
[40] T. Hiemstra, W.H. VanRiemsdijk, A surface structural approach to ion adsorption: the charge distribution (CD) model, J. Colloid Interf. Sci. 179 (2) (1996) 488–508.
[41] T. Hiemstra, P. Venema, W. Van Riemsdijk, Intrinsic proton affinity of reactive surface groups of metal (hydr) oxides: the bond valence principle, J. Colloid Interf. Sci. 184 (2) (1996) 680–692.
[42] J.G. Catalano, Z. Zhang, P. Fenter, M.J. Bedzyk, Inner-sphere adsorption geometry of Se(IV) at the hematite (1 0 0)–water interface, J. Colloid Interf. Sci. 297 (2) (2006) 665–671.
[43] K.S. Tanwar, C.S. Lo, P.J. Eng, J.G. Catalano, D.A. Walko, G.E. Brown, G.A. Waychunas, A.M. Chaka, T.P. Trainor, Surface diffraction study of the hydrated hematite (1(1)over-bar-02) surface, Surf. Sci. 601 (2) (2007) 460–474.
[44] T.P. Trainor, A.M. Chaka, P.J. Eng, M. Newville, G.A. Waychunas, J.G. Catalano, G. E. Brown, Structure and reactivity of the hydrated hematite (0 0 0 1) surface, Surf. Sci. 573 (2) (2004) 204–224.
[45] J.B. Lian, X.C. Duan, J.M. Ma, P. Peng, T.I. Kim, W.J. Zheng, Hematite (alpha-Fe_2O_3) with various morphologies: ionic liquid-assisted synthesis, formation mechanism, and properties, ACS Nano 3 (11) (2009) 3749–3761.
[46] A.K. Patra, S.K. Kundu, A. Bhaumik, D. Kim, Morphology evolution of single-crystalline hematite nanocrystals: magnetically recoverable nanocatalysts for enhanced facet-driven photoredox activity, Nanoscale 8 (1) (2016) 365–377.
[47] M. Lin, L. Tng, T. Lim, M. Choo, J. Zhang, H.R. Tan, S. Bai, Hydrothermal synthesis of octadecahedral hematite (α-Fe_2O_3) nanoparticles: an epitaxial growth from goethite (α-FeOOH), J Phys Chem C 118 (20) (2014) 10903–10910.
[48] P.M. Chapman, W.J. Adams, M. Brooks, C.G. Delos, S.N. Luoma, W.A. Maher, H. M. Ohlendorf, T.S. Presser, P. Shaw, Ecological Assessment of Selenium in the Aquatic Environment, CRC Press Inc., London, 2010, p. p 368 pp..
[49] US Environmental Protection Agency Aquatic Life Criteria for Selenium. <http://water.epa.gov/scitech/swguidance/standards/criteria/current/index.cfm>.
[50] T. Sandy, C. DiSante, Review of Available Technologies for the Removal of Selenium from Water, North American Metals Council, 2010.
[51] D.L. Plata, J.D. Hemingway, P.M. Gschwend, Polyparameter linear free energy relationship for wood char–water sorption coefficients of organic sorbates, Environ. Toxicol. Chem. 34 (7) (2015) 1464–1471.
[52] U. Schwertmann, R.M. Cornell, Iron Oxides in the Laboratory: Preparation and Characterization, Wiley-VCH Verlag GmbH, Weinheim, 2000.
[53] T. Sugimoto, Y.S. Wang, H. Itoh, A. Muramatsu, Systematic control of size, shape and internal structure of monodisperse alpha-Fe_2O_3 particles, Colloid Surf. A 134 (3) (1998) 265–279.
[54] J.G. Hamilton, R.E. Farrell, N. Chen, J. Reid, R. Feng, D. Peak, Effects of dolomitic limestone application on zinc speciation in boreal forest smelter-contaminated soils, J. Environ. Qual. 45 (6) (2016) 1894–1900.
[55] L.M. Pasquini, S.M. Hashmi, T.J. Sommer, M. Elimelech, J.B. Zimmerman, Impact of surface functionalization on bacterial cytotoxicity of single-walled carbon nanotubes, Environ. Sci. Technol. 46 (11) (2012) 6297–6305.
[56] D. Peak, Adsorption mechanisms of selenium oxyanions at the aluminum oxide/water interface, J. Colloid Interf. Sci. 303 (2) (2006) 337–345.
[57] K.O. Hodgson, J.O. Leckie, G.A. Parks, In situ X-ray absorption study of surface complexes: selenium oxyanions on o-FeOOH, Appl. Phys 42 (1971) 4290.
[58] A. Manceau, L. Charlet, The mechanism of selenate adsorption on goethite and hydrous ferric oxide, J. Colloid Interf. Sci. 168 (1) (1994) 87–93.
[59] D. Peak, D.L. Sparks, Mechanisms of selenate adsorption on iron oxides and hydroxides, Environ. Sci. Technol. 36 (7) (2002) 1460–1466.
[60] N. Jordan, A. Ritter, A.C. Scheinost, S. Weiss, D. Schild, R. Hubner, Selenium(IV) uptake by maghemite (gamma-Fe_2O_3), Environ. Sci. Technol. 48 (3) (2014) 1665–1674.
[61] C.P. Johnston, M. Chrysochoou, Mechanisms of chromate, selenate, and sulfate adsorption on Al-substituted ferrihydrite: implications for ferrihydrite surface structure and reactivity, Environ. Sci. Technol. 50 (7) (2016) 3589–3596.
[62] C.P. Johnston, M. Chrysochoou, Mechanisms of chromate adsorption on hematite, Geochim. Cosmochim. Acta 138 (2014) 146–157.
[63] N. Jordan, A. Ritter, H. Foerstendorf, A. Scheinost, S. Weiß, K. Heim, J. Grenzer, A. Mücklich, H. Reuther, Adsorption mechanism of selenium (VI) onto maghemite, Geochim. Cosmochim. Acta 103 (2013) 63–75.
[64] D. Peak, R.G. Ford, D.L. Sparks, An in situ ATR-FTIR investigation of sulfate bonding mechanisms on goethite, J. Colloid Interf. Sci. 218 (1) (1999) 289–299.
[65] T. Sugimoto, Y. Wang, Mechanism of the shape and structure control of monodispersed a-Fe_2O_3 particles by sulfate ions, J. Colloid Interf. Sci. 207 (1998) 12.